Nanoscale

PAPER

Check for updates

Quantitative analysis of weak current rectification in molecular tunnel junctions subject to mechanical deformation reveals two different rectification mechanisms for oligophenylene thiols *versus* alkane thiols†

Zuoti Xie, [ID] *‡[a,b] Ioan Bâldea, [ID] *‡[c] Quyen Van Nguyen[b] and C. Daniel Frisbie [ID] *[b]

Metal-molecule-metal junctions based on alkane thiol (CnT) and oligophenylene thiol (OPTn) self-assembled monolayers (SAMs) and Au electrodes are expected to exhibit similar electrical asymmetry, as both junctions have one chemisorbed Au–S contact and one physisorbed, van der Waals contact. Asymmetry is quantified by the current rectification ratio RR apparent in the current–voltage (*I*–*V*) characteristics. Here we show that RR < 1 for CnT and RR > 1 for OPTn junctions, in contrast to expectation, and further, that RR behaves very differently for CnT and OPTn junctions under mechanical extension using the conducting probe atomic force microscopy (CP-AFM) testbed. The analysis presented in this paper, which leverages results from the previously validated single level model and *ab initio* quantum chemical calculations, allows us to explain the puzzling experimental findings for CnT and OPTn in terms of different current rectification mechanisms. Specifically, in CnT-based junctions the Stark effect creates the HOMO level shifting necessary for rectification, while for OPTn junctions the level shift arises from position-dependent coupling of the HOMO wavefunction with the junction electrostatic potential profile. On the basis of these mechanisms, our quantum chemical calculations allow quantitative description of the impact of mechanical deformation on the measured current rectification. Additionally, our analysis, matched to experiment, facilitates direct estimation of the impact of intramolecular electrostatic screening on the junction potential profile. Overall, our examination of current rectification in benchmark molecular tunnel junctions illuminates key physical mechanisms at play in single step tunneling through molecules, and demonstrates the quantitative agreement that can be obtained between experiment and theory in these systems.

Introduction

Inspired by the original imaginative proposal by Aviram and Ratner in 1974,[1] the design of molecular tunnel junctions that rectify electrical current has been a central focus of molecular electronics researchers for decades.[2–20] Indeed, current rectifi-

[a]Department of Materials Science and Engineering, Guangdong Technion-Israel Institute of Technology, Shantou, Guangdong, 515063, China. E-mail: zuoti.xie@gtiit.edu.cn
[b]Department of Chemical Engineering and Materials Science, University of Minnesota, Minneapolis, Minnesota, 55455, USA. E-mail: frisbie@umn.edu
[c]Theoretical Chemistry, Heidelberg University, Im Neuenheimer Feld 229, D-69120 Heidelberg, Germany. E-mail: ioan.baldea@pci.uni-heidelberg.de
†Electronic supplementary information (ESI) available: Experimental and theoretical details, supplementary tables and figures. See DOI: 10.1039/d1nr04410a
‡Equal contribution.

cation is an elementary electronic function relying on electronic asymmetry between two contacts that is not only achievable in molecular systems, but also highly desirable as a first step, as rectifiers are foundational for much more sophisticated behavior in conventional electronics. It is gratifying that the molecular electronics field has made so much progress in the last 10 years on molecular tunnel diodes. Numerous researchers have reported rectification using a wide range of molecules and molecular junction platforms.[2–24] Rectification ratios (RR) of several hundred are now fairly common,[11,12,21–23,25] and record RRs of 10^5 were already reported four years ago.[26]

Understanding of rectification mechanisms in molecular diodes has also progressed and in turn this has been responsible for rational design strategies that boost performance. However, it is still not fair to say that molecular rectification in two-terminal molecular junctions is a "solved problem",

despite the tremendous recent progress. Certain core principles have emerged, for example, the need for a frontier molecular orbital to track the Fermi level shifts of one contact more strongly than the other.[4,22,25–28] This electrostatic coupling can be controlled by the spatial position of the frontier orbitals in junctions,[22,26] or by manipulating the relative sizes of the contacts.[21,29,30] Other workers, more focused on donor–acceptor architectures, invoke orbital cascades as key to current rectification.[20,23,31–33] Still others have discussed the asymmetry in the molecule-electrode electronic coupling, Γ, in the context of current rectification.[12,34–36] It seems there are several possible mechanisms for current rectification, and understanding these thoroughly and parsing which mechanisms apply in a given situation represent crucial areas for ongoing investigation.

There is also the issue of quantitative modeling. If molecular electronics is to advance as a sub-field of chemistry, it must become more quantitative. Many earlier papers on molecular diodes do not offer a model that can quantitatively simulate the current–voltage (I–V) behavior. Others do offer quantitative fits using the first principles Landauer–Buttiker formalism.[37] This description, which is foundational for molecular electronics, presents the current as an integral over orbital-assisted electron (or hole) transmission multiplied by the difference in the occupied density of states between the two (e.g., left and right) contacts. Unfortunately, nothing like the analytical Shockley equation,[38] so central to diode analysis in conventional microelectronics, and also derivable from first principles, has been widely accepted for molecular tunnel diodes. Such an equation would predict the shape of the I–V curves as a function of the basic elements of junction electronic structure, such as ε and Γ and the dimensionless voltage shift factor γ, Fig. 1A. Analytical formulas for the I–V behavior of electronic devices naturally reflect the underlying physics. For example, it is well known that the exponential dependence of current on voltage predicted by the Shockley equation is due to a built-in potential barrier at a p–n junction. In molecular electronics, sweeping all the I–V behavior under an integral as it were, can obscure some practical understanding. Of course, there may be many circumstances where such

numerical modeling is necessary. Also, deriving analytical formulas will involve approximations. Nevertheless, there is merit in identifying simple analytical formulas, derived from first principles, which can predict the observed I–V behavior for different types of molecular junctions and simultaneously return quantitative values of key electronic structure parameters. Such a tool can be convenient for experimentalists to compile systematic trends in ε, Γ, and γ (Fig. 1A) based on molecular structure in much the same way physical organic chemists compile kinetic or thermodynamic data as a function of structure.

One of us has derived a simple analytical formula for off-resonant tunneling in molecular tunnel junctions that can account for rectification behavior due to asymmetric orbital electrostatic coupling to the contacts.[39,40] In collaboration, we have found this analytical single level model (SLM), which is derived from the Landauer picture under assumptions recapped below, can beautifully capture the I–V behavior we measure for simple symmetric and asymmetric molecular tunnel junctions fabricated using the conducting probe atomic force microscopy (CP-AFM) platform, Fig. 1B.[4,41–43] Quantitative fitting of I–V characteristics with the analytical SLM using values of ε_h, for example, that are corroborated by independent measurements (such as photoelectron spectroscopy),[42–44] indicates that the SLM captures the right physics for tunneling in many simple molecular junctions. We believe it is a powerful approach that in principle should be applicable to simple molecular tunnel junctions fabricated by any method (for example ref. 45), but that generality has not yet been demonstrated.

Here we consider the differences in the current rectification behavior for molecular tunnel junctions based on self-assembled monolayers (SAMs) of alkane thiols, CnT, and oligophenylene thiols, OPTn, Fig. 1B and C. Rectification is expected for CnT and OPTn junctions because the molecules are asymmetric having a single – S functionality at one end that is bonded to one electrode. Experimentally, the rectification is observed to be weak, and indeed other authors have reported weak rectification for CnT and OPTn junctions using different junction testbeds.[4,14,46–48] In a prior publication, we have explained both the direction and magnitude of current
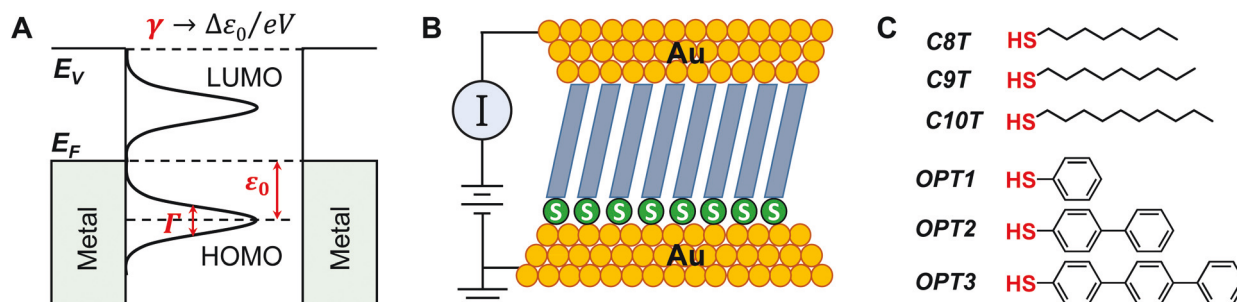

Fig. 1 (A) Typical junction electronic structure with key parameters: energy level offset ε_0 (HOMO level relative to the Fermi level), molecule–electrode coupling strength Γ, level shift coefficient γ, and level shift $\Delta\varepsilon_0 = \varepsilon_0(V \neq 0) - \varepsilon_0(V = 0)$. (B) Scheme of the CP-AFM molecular junction. An Au-coated AFM tip is brought into contact with a SAM of (C) alkane thiol (CnT, n = 8, 9, 10) and oligophenylene thiol (OPTn, n = 1, 2, 3) of various lengths on an Au coated substrate.

rectification in CnT junctions, and we have shown that the SLM is able to quantitatively describe the I–V characteristics;[4,43] the main results of that study will be briefly recapped later. In this paper, our focus is on comparison of weak rectification behavior in CnT $vs.$ OPTn junctions precisely because their rectification properties are notably different even though they appear to have similar chemical asymmetries. Further, because we examine rectification in molecular junctions fabricated using the conducting probe atomic force microscopy (CP-AFM) approach, we are able to stretch both types of junctions while recording their I–V characteristics. Again, we find that the junction behavior under stretching is remarkably different.

Quantitative analysis of these differing behaviors turns out to be very instructive. Using the analytical SLM and supporting quantum chemical calculations, we are able to describe quantitatively the experimental electrical transport data for CnT and OPTn junctions in both stretched and unstretched states. We find two distinct, but very general rectification mechanisms apply. In CnT junctions, the rectification is based on the Stark effect[4,9,49] ($e.g.$, field-induced electron polarization leading to an orbital energy shift; note that the nominal fields in junctions are large, of order 10^7 V cm^{-1}), whereas in OPTn junctions the dominant mechanism involves spatially-dependent electrostatic coupling of the transport orbital (more specifically its "center of charge") to the junction potential profile – this has been referred to before as the potentiometer effect.[4,50–55] In both mechanisms, the energy of the principal transport level ($e.g.$, HOMO for CnT[43] and for OPTn[42]) shifts as the junction voltage is swept. The HOMO level shifting in turn leads to rectification. However, which type of coupling (field or potential) dominates in a given junction – the Stark shift or the potentiometer shift – depends on the specific molecules in question. In this sense, comparison of CnT and OPTn junctions is particularly judicious as the HOMOs of these molecules have very different spatial characteristics and Stark shift sensitivities, as will be shown. It is also the very different spatial extents of the HOMOs for CnT and OPTn that lead to the contrasting rectification behaviors on stretching.

In addition to clarifying the rectification mechanisms in CnT and OPTn junctions, our analysis also allows quantitative assessment of electrostatic screening and its impact on the junction potential profiles. Significant potential is dropped at the contacts because of screening, and quantitative prediction of the potential drops is possible by comparison of experimental results with an accurate physical model for the junction I–V behavior.

We emphasize that our motivations in this work are fundamental, and the simplicity of the junctions ($i.e.$, their small structural asymmetry) does not allow record-setting rectification ratios to be obtained. However, we find that our combined experimental and theoretical study provides substantial clarity on rectification mechanisms in simple molecular tunnel junctions and demonstrates that quantitative understanding of single step tunneling in these systems is possible using analytical theory supported by quantum chemical calculations.

Methods

Materials

Au nuggets (99.999% pure) were purchased from Mowry, Inc. (St Paul, MN). Evaporation boats for Au and Cr evaporation rods were purchased from R. D. Mathis (Long Beach, CA). Silicon (100) wafers were purchased from WaferNet (San Jose, CA). The alkane thiols (CnT) and oligophenylene thiols (OPTn) used in this study were purchased from Sigma-Aldrich Company. AFM probes (DNP 10 SiN probes) were purchased from Bruker AFM Probes.

Conducting tip and sample preparation

Conductive AFM tips used for current measurements were prepared by coating Au at a base pressure of 10^{-7} Torr using a thermal evaporator placed in a N$_2$-filled glove-box. Au was deposited to a thickness of 50 nm at a rate of 0.5–1.0 Å s^{-1} with a ~5 nm Cr adhesion layer. They were immediately transferred to another N$_2$-filled glove-box to carry out the I–V measurements without exposure to air. The radius of the Au coated AFM tip is expected to be ~50 nm.[56] For template-stripped flat Au substrates, 500 nm of Au was directly deposited onto clean Si wafers in a high vacuum e-beam evaporator. We then glued Si chips (~1 cm^2) onto the metal surface using epoxy. The epoxy layer was cured by placing the wafers in an oven at 120 °C for 1 h. The flat Au substrates were peeled off from the silicon surface and immersed in an ethanol solution of molecules at a concentration of ~1 mM for 20 h. Afterward, the samples were rinsed with ethanol and dried with flowing N$_2$.

Previously, we have characterized CnT and OPTn SAMs by XPS, ellipsometry, AFM, Rutherford backscattering spectrometry, and nuclear reaction analysis to obtain the thickness, tip-SAM adhesion force, and molecular coverage of SAMs respectively.[42,57] The Maugis-Dugdale (MD) model of contact mechanics[56] is employed to calculate the contact area and the actual number of the molecules per junction.[56,57]

Transport measurements

All the electrical measurements were performed in an N$_2$ filled glove box with H$_2$O and O$_2$ < 1 ppm. To form the CP-AFM junction, the SAM coated template-stripped flat Au substrate was first mounted on the AFM sample stage, then an initial compressive force (F = +1 nN) was applied to the Au-coated AFM tip to create the contact with the SAM surface (Fig. 1B). After the contact was established, the applied force was tuned (to negative values) by changing the cantilever deflection setpoint. The value of the rupture or pull-off force was found to be similar for both CnT and for OPTn-based SAMs and independent of molecular size n. Current–voltage measurements were collected at different applied forces. Voltages were applied to the AFM tip with a Keithley model 236 electrometer operated in "DC mode" with the sample grounded. Positive biases ($V \equiv V_t - V_s > 0$) correspond to situations wherein the tip's potentials V_t are higher than the substrate's potentials V_s. Voltage spanned ±1.5 V for CnT junctions and ±1.2 V for OPTn junctions. 50–200 I–V curves were collected for each type of junction.

Quantum chemical calculations

Geometry optimization for stretched OPTn molecules subject to tensile (compressive) mechanical forces $F < 0$ ($F > 0$) was accomplished by fixing the distance $d \equiv d(\text{S, C})$ between the S and C atoms at the two molecular ends at values gradually increased (decreased) with respect to the value (13.24 Å) at $F = 0$ at the B3LYP/6-311++G(D, P) level of theory. This framework was also utilized to obtain the HOMO densities (Fig. 6) and electric potential profiles (Fig. 7, S5–S8†). Computations to obtain the HOMO energies of isolated OPTn and CnT molecules in the presence of an applied bias (Fig. 5) were based on the *ab initio* outer valence Green's function (OVGF) method.[58,59] These quantum chemical calculations were carried out with GAUSSIAN 16 [60] on the bw-HPC platform,[61] as done earlier *e.g.* for alkane thiols in ref. 4, where more details can be found.

Results and discussion

Theoretical methods for transport calculations

Measured transport data were processed within the single-level model (SLM), which expresses the current as follows:[40,62]

$$I = GV \frac{\varepsilon_\text{h}^2}{[\varepsilon_0(V)]^2 - (eV/2)^2} \qquad (1)$$

Here, G is the low bias conductance and

$$\varepsilon_0(V) = E_\text{HOMO}(V) - E_\text{F} = -\varepsilon_\text{h} + \gamma eV \qquad (2)$$

is the HOMO energy offset relative to metal's Fermi energy E_F (N.B.: $\varepsilon_0(V = 0) \equiv -\varepsilon_\text{h} < 0$) which is shifted by the applied bias V with respect to the value $\varepsilon_0(V = 0) \equiv -\varepsilon_\text{h}$ in the unbiased junction by an amount quantified by the dimensionless shift parameter γ. Eqn (1) enables one to express the HOMO-Fermi energy offset ε_h (N.B.: $\varepsilon_\text{h} > 0$) and the bias-driven HOMO shift parameter γ in terms of the transition voltages $V_{\text{t}+}$ and $V_{\text{t}-}$ at positive and negative bias polarity as follows[4,40]

$$\varepsilon_\text{h} = 2 \frac{e|V_{\text{t}+}V_{\text{t}-}|}{\sqrt{V_{\text{t}+}^2 + 10|V_{\text{t}+}V_{\text{t}-}|/3 + V_{\text{t}-}^2}} \qquad (3)$$

$$\gamma = -\frac{1}{2} \frac{V_{\text{t}+} + V_{\text{t}-}}{\sqrt{V_{\text{t}+}^2 + 10|V_{\text{t}+}V_{\text{t}-}|/3 + V_{\text{t}-}^2}} \qquad (4)$$

It is the nonvanishing value of γ that makes the MO energy offset at positive (+V on the tip) and negative (−V on the tip) bias different. This, in turn, makes current magnitudes $I(V)$ and $|I(-V)|$ different from each other, which implies current rectification: $\text{RR}(V) \equiv I(V)/|I(-V)| \neq 1$.

Current–voltage characteristics of CnT and OPTn

As expected in view of their chemical asymmetry, our measurements revealed that both CnT and OPTn junctions possess I–V curves asymmetric with respect to the origin. Typical curves measured for non-stretched CnT and OPTn junctions are depicted in Fig. 2A and B. Although the chemical asymmetries

of the CnT and OPTn junctions are similar (one chemical contact to the substrate and one physical contact to the tip), the two junctions exhibit opposite asymmetry in I–V curves. The C8T junction currents for positive tip biases (sample is grounded) are smaller than currents for negative biases, while the contrary is true for OPT3 junctions. Consequently, as presented in Fig. 2C, the RR as a function of bias trends in opposite directions for the two cases; RR(V) < 1 for C8T, while RR(V) > 1 for OPT3. In the absence of stretching, we measured for each CnT junction a rectification ratio at 1.5 V amounting to about 0.7 (see Fig. 2D). This value agrees with those reported in previous studies.[4,14] For OPTn junctions, we found an average rectification ratio RR ≈ 2–3 at 1.2 V (also shown in Fig. 2D).

We have reported that mechanical stretching has an impact on the low bias conductance G of CnT junctions that is different from that on OPTn junctions.[57] Here, we show that RR is also affected by stretching in a qualitatively different way for the two types of junctions. This is illustrated by the representative curves depicted in Fig. 3. Within the entire range of stretching forces ($F > -10$ nN) that can be sampled in the experiment (rupture occurs at more negative tensile forces), the asymmetry of the I–V curves recorded for C8T junctions does not change, Fig. 3A and C; the rectification ratio RR is independent of F, Fig. 3E. In contrast, RR is strongly affected by tensile forces for OPTn junctions, as visible by inspecting the blue traces in Fig. 3B and D. The different rectification behavior is summarized in Fig. 3E, which shows that the initially larger RR for OPTn junctions becomes progressively smaller as the magnitude of the tensile force increases; RR eventually disappears (RR → 1) at the end of the stretching process. At first, the rectification ratio RR decreases slowly with increasing (more negative) tensile force, but the reduction in RR becomes more rapid beyond $F \approx -8$ nN (Fig. 3E).

According to the SLM, current rectification is the result of bias driven shifting of the HOMO, which is the dominant transport channel both in CnT and in OPTn junctions.[4,42,57] Higher currents occur when the applied bias shifts the HOMO energy closer to the Fermi level; lower currents occur when the bias shifts the HOMO further away from the Fermi energy (this will be discussed in detail in the Discussion). The dimensionless (HO)MO level shift coefficient γ quantifies the magnitude and sign of the shift and thus the propensity for rectification (eqn (2)). Crucially, γ can be determined from the experimental I–V curves by extracting the transition voltages at positive ($V_{\text{t}+}$) and negative ($V_{\text{t}-}$) polarities and inserting these into eqn (4).[4,42,43] From the values of $V_{\text{t}\pm}$ (see Fig. S1 in the ESI†) indicated in Fig. 2A and B, the dependence of γ on the stretching force F is derived. The results are presented in Fig. 3F. As observable there, for C8T junctions (which are representative of all CnT junctions), γ is negative and within error independent of the tensile force ($\gamma \approx -0.03$). For OPT3 junctions (OPT1 and OPT2 junctions behave similarly), on the other hand, γ is positive and switches from a plateau regime ($\gamma \approx +0.06$, RR ≈ 3) for forces up to $F \approx -6$ nN, to a sharply decreasing regime beyond $F \approx -8$ nN, ending with γ near zero, corresponding to
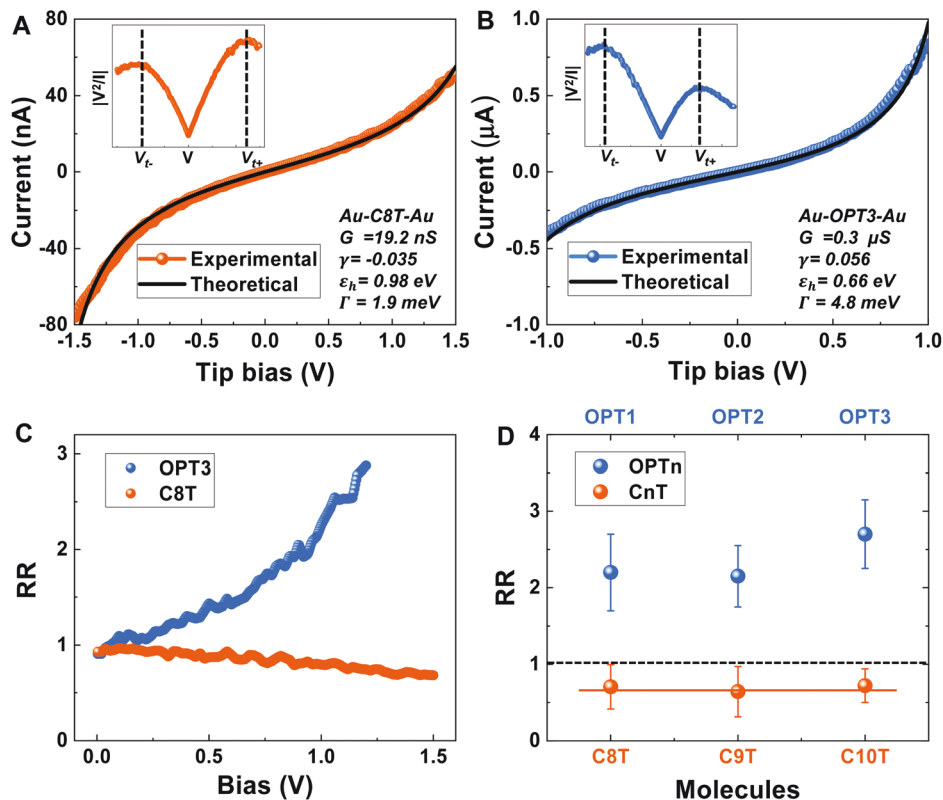
Fig. 2 Typical current–voltage characteristics measured for non-stretched (A) C8T and (B) OPT3 CP-AFM junctions with Au electrodes are asymmetric with respect to the origin. The insets are the TVS spectra of C8T and OPT3 junctions. Fits to the SLM are shown in black. The three extracted parameters for each junction are listed: low bias conductance G ($1/R$), the energy offset ε_h and energy level shift factor γ. The calculated coupling strengths Γ ($= \varepsilon_h \sqrt{G/NG_0}$, where $G_0 = 2e^2/h$ is the quantum conductance) are also provided. Note that G is determined by the (ohmic) low bias conductance and ε_h and γ are determined from TVS spectra and eqn (3) and (4). (C) Rectification ratio RR for non-stretched OPT3 and C8T junctions as a function of bias and (D) RR of non-stretched OPTn (at $V = 1.2$ V) and CnT (at $V = 1.5$ V) as a function of n.

complete loss of the I–V asymmetry ($\gamma \rightarrow 0$, RR $\rightarrow 1$) as the contact rupture point ($F \approx -10$ nN) is approached. The behaviors of γ for both C8T and OPT3 in Fig. 3F reflect the behaviors of RR in Fig. 3E because RR depends on γ via eqn (1), (2) and (4).

To end this section, we note that our basic theoretical formula to analyze rectification, eqn (4), relies on the assumption that the applied bias V causes a HOMO energy shift that linearly depends on V, cf. eqn (2). To check the correctness of this basic assumption against our transport data, we also attempted to process our I–V measurements by means of eqn (1) and (2) modified to include possible higher order contributions (γ_2, γ_3, ...) to the bias-driven HOMO level shift, which cannot be ruled out a priori. So, we replaced $\gamma V \rightarrow \gamma V + \gamma_2 V^2 + \gamma_3 V^3$... in the right hand side of eqn (2) and incorporated this modification into eqn (1). Our I–V data do support eqn (2) as is, i.e. with $\gamma_{2,3,...} \equiv 0$. For the analysis that follows, this is an important finding; it validates a theoretical approach wherein, for the entire bias range sampled in experiments, the impact of V on the HOMO energy is accounted for within the first-order perturbation theory. To avoid confusion, we emphasize that the aforementioned refers to the (linear) V-dependence of the HOMO energy and not to the current, whose nonlinear

dependence on V was obviously accounted for (cf. Fig. 2 and eqn (1)).

To analyze the two main differences between the CnT and OPTn experimental findings presented above (i.e., opposite current rectification direction and different impact of mechanical deformation), we corroborate information extracted from the charge transport data using the SLM analysis – which we have validated earlier both for CnT[43] and OPTn[42] junctions – with ab initio results of quantum chemical calculations.[59,63]

Opposite direction of the current rectification in unstretched CnT and OPTn junctions

As noted above, given the similar chemical asymmetry of the CnT and OPTn molecules (one thiol group at one molecular end only), the opposite direction of the current rectification – currents for positive biases (sample is grounded) lower than currents for negative biases in CnT junctions (RR < 1) but higher in OPTn junctions (RR > 1) – seems surprising and deserves explanation.

Within the SLM, current rectification is the consequence of the fact that, as expressed by eqn (2), the applied bias V causes an energy shift of the dominant transport channel (which is the HOMO in both types of junctions[42,43,64–66]). As sketched in
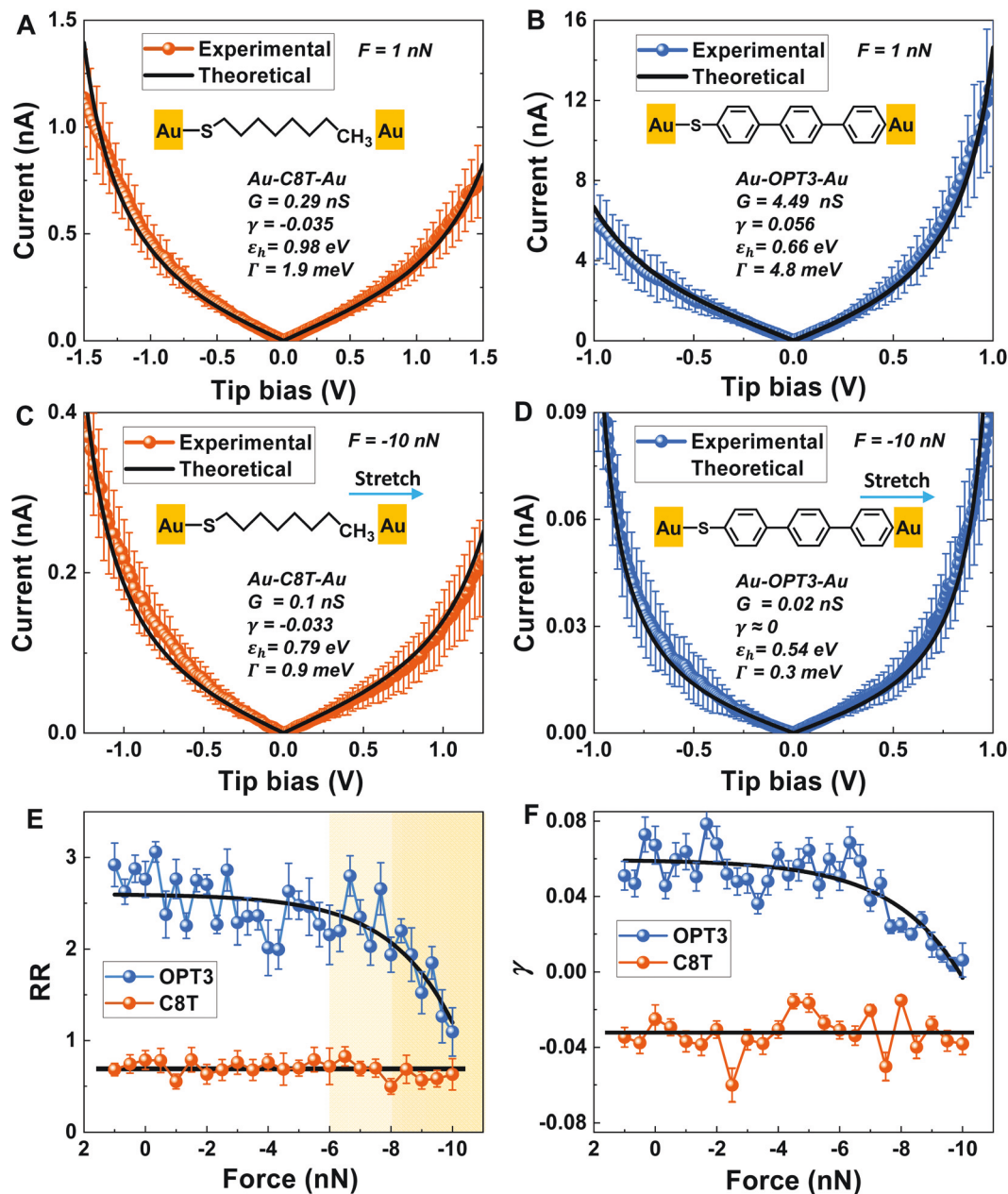
Fig. 3 Representative $I-V$ curves, with current normalized per molecule (*cf.* ref. 57) for (A and C) C8T and (B and D) OPT3 junctions under applied force $F = 1$ nN (small compression) and $F = -10$ nN (tension). Note that the absolute value of the current is shown at negative voltages to make symmetry and asymmetry more apparent. (E) Current rectification ratio (RR) for OPT3 (at $V = 1.2$ V) and C8T (at $V = 1.5$ V) junctions as a function of the mechanical stretching force F. RR *vs.* F for OPT2, C9T, and C10T are shown in Fig. S2 in the ESI.† (F) Dependence of the extracted shift parameter γ on the stretching force F. The black lines in panels E and F are a guide for the eye.

Fig. 4, the sign of γ dictates the direction of the current rectification. For $\gamma > 0$, Fig. 4A, the HOMO energy offset at positive bias polarity (+V on the tip) is smaller than at negative bias polarity (−V on the tip). That is, at positive biases the HOMO is closer to the Fermi level than at negative biases, which makes currents at positive biases larger than currents at negative biases and hence RR > 1. This situation is opposite for the case $\gamma < 0$, for which a similar argument yields RR < 1, Fig. 4B. Whether γ is positive or negative depends on the specific junc-

tion in question. Loosely speaking, for a molecule embedded in a junction, the HOMO energy shift can be disentangled into a field-driven level shift due to the Stark effect and a potential-driven level shift emerging from convolution of the orbital position (its center of charge) and the potential profile across the junction. The latter mechanism has been intuitively referred to as the potentiometer rule.[4,50–55] (Point of clarification: it is common in solid-state theory to distinguish between "voltage-driven" conduction processes, such as tunneling, and
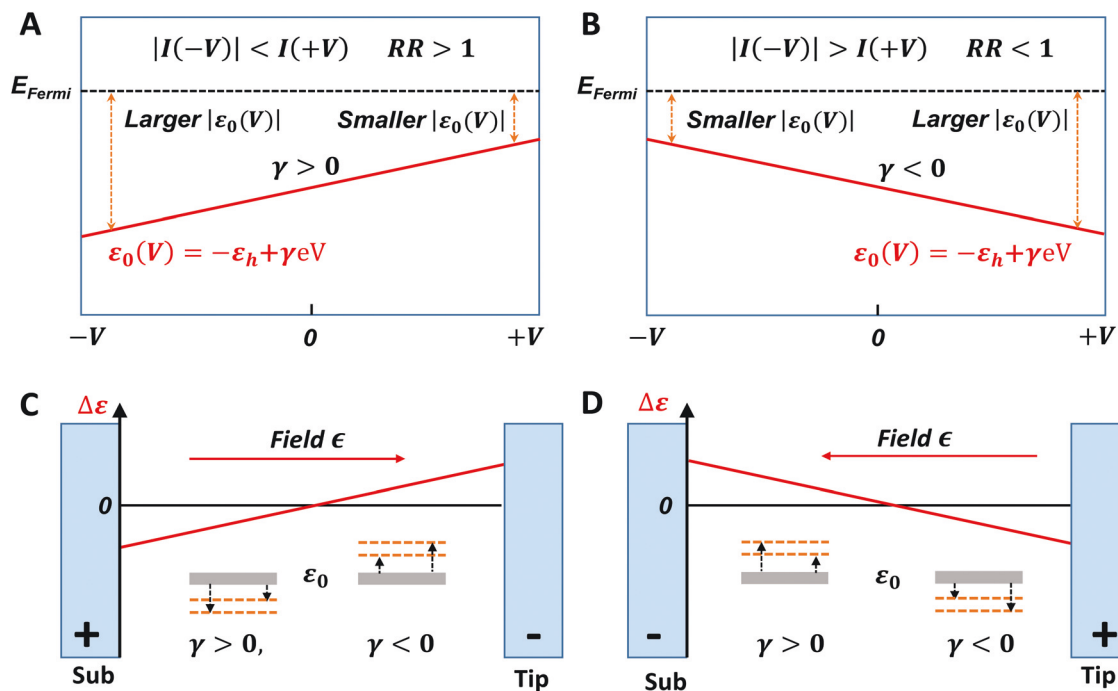
Fig. 4 Understanding current rectification based on HOMO level shifts ε_0 (V) and the potentiometer concept (voltage driven level shifts). (A) Bias dependent level shift in the case where $\gamma > 0$. The x-axis is tip bias V. In this case RR > 1 as indicated because a smaller offset ε_0 (V) at +V yields more tunneling current than at −V. (B) Bias dependent level shift in the case where $\gamma < 0$. Now RR < 1. (C) Illustration of level shifting under the potentiometer rule; note that the x-axis now corresponds to distance from the substrate, and the red line shows the simplest, often-assumed potential profile. Two hypothetical HOMO orbitals are shown, one left of center of the junction, the other right of center. The two orbitals shift in opposite directions for the same bias $V < 0$. The corresponding γ values of the two orbitals are indicated, see text. (D) Same illustration as in (C), but with $V > 0$.

"field-driven" processes such as ohmic conduction. The terminology refers to the distinction in primary driving force. Here we use these descriptors to highlight the different physics of the two level shifting effects.)

In the form utilized so far in the literature,[4,50–55] discussion of the potentiometer rule is couched in terms of a point-like (HO)MO and a linear (vacuum-like) potential profile, with the potential at any point (Fig. S3†) being an interpolation between the potentials of the substrate and the tip (we will comment below on deficiencies of this assumption). In such a situation, the HOMO tracks the Fermi level of the closest electrode, and this behavior determines the current rectification and the sign of γ. Then, simple geometrical considerations (see ESI† and ref. 51 bearing in mind the sign convention in eqn (2) (opposite to ref. 51) that positive bias corresponds to positive voltage on the tip) allow us to express γ simply in terms of the junction's length d and the HOMO location z_{HOMO} relative to junction's center at z_0

$$\delta\varepsilon_0(V) = e\frac{z_0 - z_{HOMO}}{d}V \Rightarrow \gamma = \frac{z_0 - z_{HOMO}}{d} \quad (5)$$

In agreement with eqn (5), Fig. 4C illustrates the bias driven level shifts for two cases, i.e., a HOMO orbital closer to the substrate (left of center, $z_{HOMO} < z_0$) and a HOMO closer to the tip (right of center, $z_{HOMO} > z_0$). As shown, when negative bias is applied to the tip, the level shift is positive (up) for the HOMO located closer to the tip and negative (down) for the

HOMO located closer to the substrate. In other words, the levels track the Fermi level of the closest electrodes, respectively. Because Fig. 4C corresponds to $V < 0$, it follows that $\gamma > 0$ for the left case and $\gamma < 0$ for the right case (see eqn (2)). Fig. 4D illustrates the level shifts for the same two hypothetical orbitals when $V > 0$. Note also that RR > 1 for the left-of-center situation and RR < 1 for the right-of-center case. The scenarios in Fig. 4C and D are the expected behavior when field-driven Stark effects are negligible and the potentiometer rule (i.e., a voltage driven shift) dominates.

We return now to a comparison of CnT and OPTn junctions. Although the HOMO of CnT is localized on the anchoring thiol group (see wavefunction depicted in Fig. 5A) and hence lies very close to the substrate, as already noted,[4] the charge transport in CnT junctions is characterized by $\gamma < 0$. This is at odds with the predictions in Fig. 4C and D just discussed. This counterintuitive behavior[4,51] – where the CnT HOMO apparently tracks the more distant tip electrode (Fig. S4C and D†) – is the result of a strong Stark effect, which gives rise to an opposite level shift[4] that prevails over the potentiometer rule expectation. The OVGF computed Stark shift for the CnT HOMO is shown in Fig. 5B. The shift is quite pronounced, over 0.5 eV for fields of ~10^7 V cm^{-1}, at applied biases of ±1 V. As noted in the Introduction, we have described the CnT rectification behavior without stretching previously,[4] so below we focus on the OPTn rectification.
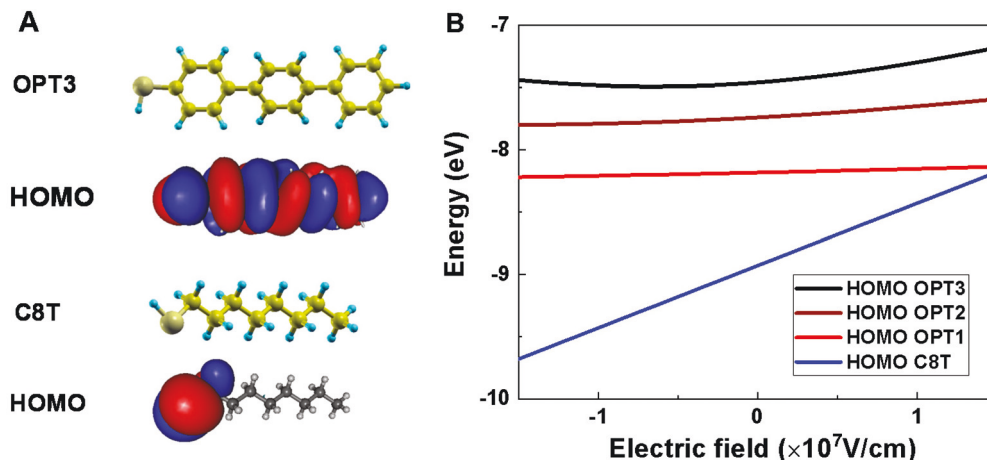
Fig. 5 (A) Molecular structures and HOMO spatial distributions for OPT3 and C8T. (B) Stark effect behavior is shown by the dependence of HOMO energies on electric field E (and thus bias V) obtained from OVGF calculations. Notice the negligible dependence on E (and thus V) of the curves for OPTn molecules which contrasts with the strong dependence exhibited by C8T shown here as representative for alkane thiols. Conversion between E and V is obtained by $E = V/L$, where L is the S-to-terminal C molecular length.

One should first note that an OPTn HOMO shift due to a field-driven Stark effect in the opposite direction to that in CnT, in apparent agreement with the potentiometric rule expectation, cannot a priori be excluded. Our OVGF calculations to check this possibility are presented in Fig. 5B and reveal that the field-dependence of the OPTn HOMO energies is very weak; whether upwards or downwards, these field-driven shifts, of much smaller magnitude than in CnT, are too small for Stark effects to come into play when quantitatively analyzing rectification for OPTn. It is this altogether ineffective Stark effect that makes the potentiometer rule trend dominant for OPTn, resulting in positive values of γ and current rectification values RR > 1.

Still, the question that immediately arises is how can the potentiometer rule hold for OPTn, given the fact that, in contrast to the high asymmetry of the CnT HOMO spatial distribution (cf. Fig. 5A), the asymmetry of the OPTn HOMO is much less pronounced. In fact, although it is not readily observable in the orbital spatial distribution for OPT3 depicted in Fig. 5A, the asymmetry is apparent if one inspects the HOMO density projected along the molecular axis z which is depicted in Fig. 6.

$$\rho_{HOMO}(z) \equiv \frac{\int \rho_{HOMO}(x,y,z)dxdy}{\int \rho_{HOMO}(x,y,z)dxdydz} \quad (6)$$

More quantitatively, quantum chemical calculations show that HOMO's center of charge location on OPT3's molecular axis

$$z_{HOMO} \equiv \langle z \rangle = \frac{\int z\rho_{HOMO}(x,y,z)dxdydz}{\int \rho_{HOMO}(x,y,z)dxdydz} = \int z\rho_{HOMO}(z)dz \quad (7)$$

is closer to the S atom than to the C atom at the opposite molecular end ($z_{HOMO} - z_S = 4.46$ Å versus $z_C - z_{HOMO} = 8.78$ Å, respectively), Fig. 6A. If we now apply eqn (5) using these values and associate the HOMO position with its center of

charge, based on the conventional potentiometer rule (PR) we find a value $\gamma_{PR} \approx +0.16$. The positive sign of this quantity is in agreement with the experimental rectification direction. Less satisfactory is the magnitude, which is roughly three times larger than the experimental value ($\gamma_{expt} \approx 0.06$). At first glance, it seems necessary to be resigned to this discrepancy between theory and experiment, noting that deviations of previous theoretical γ-estimates from experiment are much larger (see discussion in ref. 40). Fortunately, however, it turns out that full quantum chemical calculations can close the gap.

In its most general formulation, the potentiometer rule convolves the spatial location of an orbital density $\rho(x,y,z)$ with the potential profile $v(x,y,z)$ across the junction (see section "Notations and some useful relations" in the ESI† for the meaning of various notations utilized). This is schematically depicted in Fig. 4C and D and expressed quantitatively in eqn (8)

$$\delta\varepsilon_0(V) = -e\frac{\int \rho_{HOMO}(x,y,z)v(x,y,z)dxdydz}{\int \rho_{HOMO}(x,y,z)dxdydz}; \gamma = \frac{\delta\varepsilon_0(V)}{eV} \quad (8)$$

As discussed in more detail in the ESI,† eqn (8) is a general result of the first-order perturbation theory (that we have validated, see the last paragraph of Results section) that holds for arbitrary HOMO spatial distributions $\rho_{HOMO}(x,y,z)$ and potential profiles $v(x,y,z)$. Computing the convolution in eqn (8) requires state-of-the-art quantum chemical calculations in which the electron distribution and the potential profile are self-consistently solved at each applied bias (see ESI†). The results of our self-consistent quantum chemical calculations (i.e. solving the coupled system of Schrödinger and Poisson equations) for $\delta\varepsilon_0(V)$ obtained via eqn (8) are depicted by red points in Fig. 7A. The (positive!) slope of the virtually perfect straight line deduced via eqn (8) on which these points lie (cf. eqn (2)) provides us with a theoretical estimate $\gamma_{theor} \approx +0.05$,
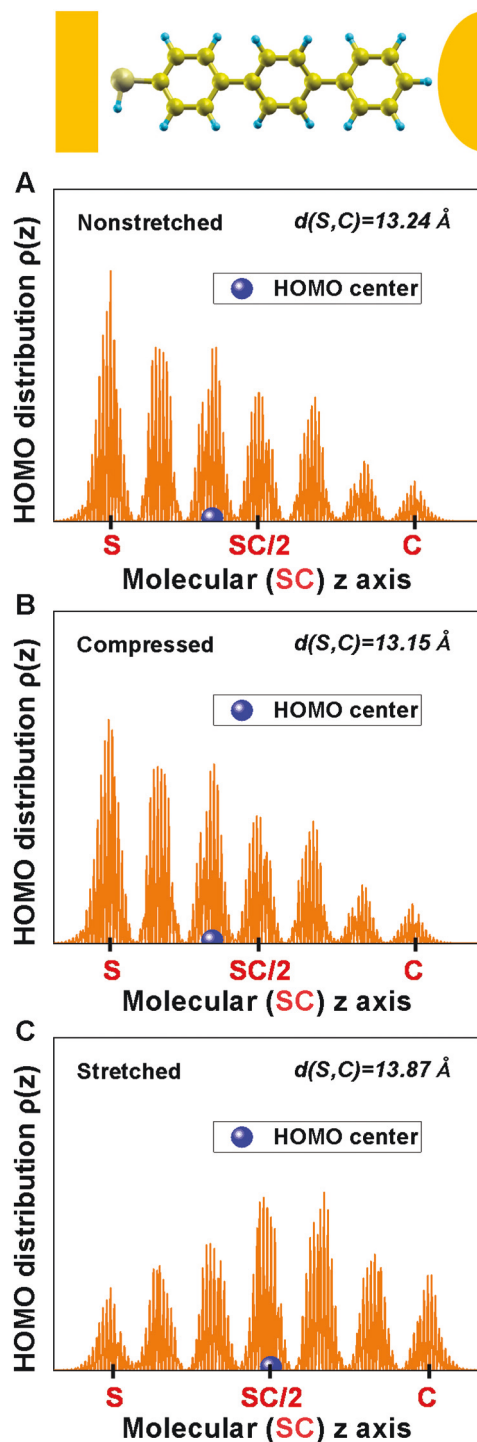
Fig. 6 Projected HOMO density along the OPT3 molecular axis. The HOMO spatial distribution integrated over transverse directions (eqn (6)) reveals that HOMO's center of charge (blue dot on x-axis) is closer to the S atoms for (A) nonstretched and (B) compressed OPT3 molecules. (C) The center of charge moves toward the center of the molecule for stretched molecules, which eventually makes rectification vanish as the junction rupture point is approached.
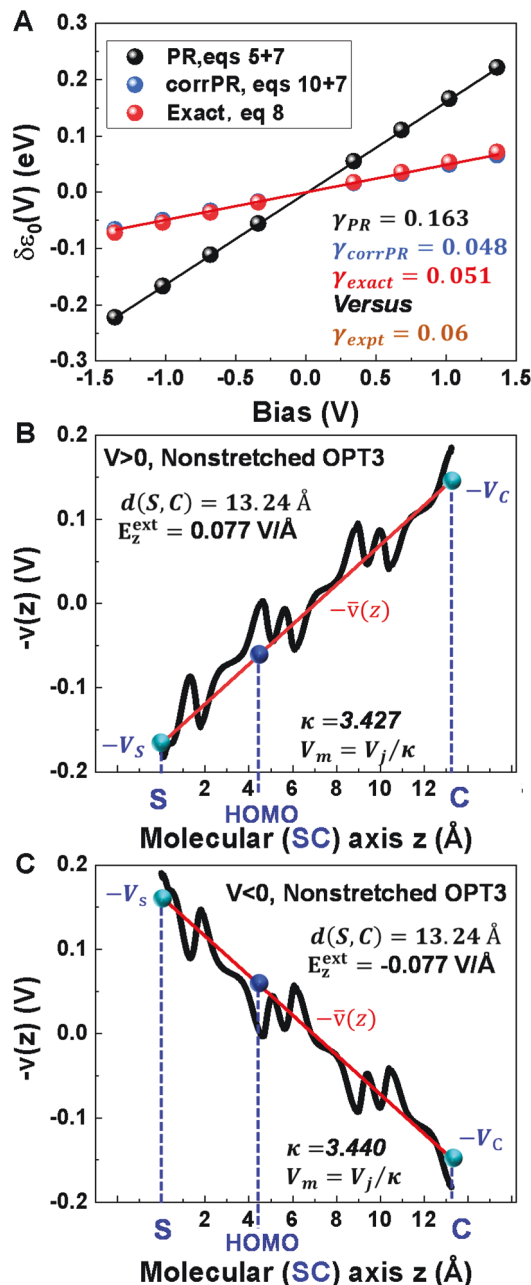

Fig. 7 Results for OPT3 junctions. (A) The HOMO energy shift $\delta\varepsilon_0$ vs. bias V computed exactly by means of eqn (8) (red, labeled "exact"). Also shown are estimations of $\delta\varepsilon_0$ by using the potentiometer rule both in its conventional form in eqn (5) (black) and corrected with molecule's dielectric constant κ (eqn (10)) (blue). See text for details. The shift parameters γ correspond to the slopes of these plots and their values are shown in the inset. (B) The computed microscopic potential $v(z)$ along the molecular axis z (solid black curve) and its coarse grain average $\bar{v}(z)$ (solid red line). Its slope is smaller than the value of the external (unscreened) field E_z^{ext} by the factor κ (molecule's dielectric constant). (C) Same as B but for negative bias V. Depicting potentials with reversed sign on the ordinate axis in panels B and C (notice the minus sign in the y-axis label) facilitates understanding that the HOMO bias-driven shifts follow the direction expected in the potentiometer rule scenario.

which excellently agrees with the experimental value $\gamma_{\text{expt}} \approx$ +0.06 (*cf.* Fig. 3F).

To obtain the bias-driven HOMO shift from eqn (8) we used potential profiles $v(z)$ obtained from self-consistent quantum chemical calculations. As visible by inspecting eqn (S12)† and the discussion related to it in the ESI,† $v(z)$, a HOMO-dedicated property, represents the average of the microscopic potential $v(x,y,z)$ over the (x,y) transverse coordinates weighted with the HOMO spatial density ρ_{HOMO}. Rather than the average over the whole SAM, it is just what we need to quantify the bias-driven HOMO shift; see eqn (8). Curves for $v(z)$ are the solid black lines shown in Fig. 7B and C as well as those depicted in Fig. S5, S6, and S8 of the ESI.† Apart from short-range irregularities which reflect the discrete (atomistic) molecular structure, the linear trend of the curves for $v(z)$ in Fig. 7B and C is readily recognizable; these are the red straight lines defining the coarse grain average potential $\bar{v}(z)$ of Fig. 7B and C (the value V = 1.02 V (corresponding to E_z = 15 u = 0.077 V Å^{-1}) chosen in Fig. 7B and C, which seems strange, is due to the fact that the program utilized for quantum computations (Gaussian[60]) only accepts values of the electric field E expressed as integer numbers of the (Gaussian) unit u = 10^{-4} a.u. = 0.00514 V Å^{-1}.) The slope of $v(z)$ allows us to define a coarse grain average "internal" field E_{internal} embodying intramolecular screening effects which linearly scale with E_{ext}: $E_{\text{internal}} = E_{\text{ext}}/\kappa$. The constant of proportionality defines molecule's dielectric constant κ, which also provides us with a relationship between the (external) bias $V_{\text{junction}} \equiv V$ applied to junction and the bias V_{molecule} responsible for HOMO level shift:

$$V_{\text{molecule}} = V_{\text{junction}}/\kappa \tag{9}$$

From the above remark on the average potential $v(z)$, it should be clear that κ does account for the (screened) potential felt by the HOMO; by no means should it be confused with the dielectric constant of the SAM.

If we now correct the conventional potentiometer rule that assumes an unscreened vacuum-like linear potential in the light of eqn (9), that is, by replacing $V \equiv V_{\text{junction}}$ in eqn (2) and (5) and (S8)† with V_{molecule} of eqn (9) we arrive at the following form

$$\varepsilon_0(V) \equiv -\varepsilon_{\text{h}} + \delta\varepsilon_0(V)$$
$$= -\varepsilon_{\text{h}} - e\bar{v}(z) = -\varepsilon_{\text{h}} - \frac{eV(z_{\text{HOMO}} - z_0)}{\kappa(z_{\text{C}} - z_{\text{S}})} \tag{10}$$

This allows expression of γ as follows

$$\gamma = \frac{(z_0 - z_{\text{HOMO}})}{\kappa d} \tag{11}$$

Results for OPT3 obtained as indicated above are also presented in Fig. 7A ("corrected PR", blue points). As visible there, by correcting the potentiometer rule expressions to account for intramolecular screening embodied in the value $\kappa \approx 3.4$ computed microscopically, the value $\gamma_{\text{corrPR}} \approx 0.048$ is in very good agreement with the "exact" theoretical estimate $\gamma_{\text{corrPR}} \approx 0.051$ and the experimental value $\gamma_{\text{expt}} \approx 0.06$. Of course, the dielec-

tric screening effect is intrinsically accounted for when solving eqn (8) self-consistently, which is why the exact calculation produced excellent agreement with the experimental value of γ. Note also in Fig. 7A that the uncorrected (no screening) potentiometer rule calculation using eqn (5) and (7) (black points) over-predicts the voltage shift.

To summarize this part, the different current rectification exhibited by CnT and OPTn junctions is the result of the interplay between the field-driven Stark effect and the potential-driven shifts triggered by the potentiometer rule. The former dominates in CnT and, counterintuitively (*cf.* ref. 4) yields a negative value of γ (*cf.* Fig. 2A). At the highest positive bias (V = +1.5 V) used for the C8T junction of Fig. 2A, the HOMO level lies 1.02 eV below the Fermi level (ε_{0+} = −1.02 eV, *cf.* eqn (2)). So, it is more distant than the HOMO level at the opposite polarity (V = −1.5 V), which lies only 0.93 eV below the Fermi level (ε_{0-} = −0.93 eV, *cf.* eqn (2)). This renders the current at positive bias smaller than the current at negative polarity $I_+ < |I_-|$, and this translates into a rectification RR < 1 (specifically, RR (+1.5 V) $\approx$ 0.7, *cf.* Fig. 2C) whose direction is opposite to the potentiometer rule. By contrast, the Stark effect is negligible in OPTn, where the potentiometer rule dominates and makes γ positive. When appropriately corrected (κ > 1), the potentiometer rule can quantitatively reproduce (both the sign and the magnitude of) the key parameter γ quantifying the experimental current rectification. As the bias gradually increases from zero (bias on tip), this makes RR become larger and larger than unity in OPTn junctions, opposite to CnT junctions wherein RR becomes lower and lower than unity, Fig. 2C. (We note here that RR ($V \to 0$) $\to$ 1 (*cf.* Fig. 2C) is a result that holds for any transport mechanism by tunneling (see the section of "Demonstration that RR ($V \to 0$) = 1 holds for any transport mechanism by tunneling" in the ESI†)). To refer again to a specific case (Fig. 2), at the highest positive bias (V = +1.2 V) used for the OPT3 junction of Fig. 2B, the HOMO level at 0.59 eV below the Fermi level (ε_{0+} = −0.59 eV, *cf.* eqn (2)) is less distant than the HOMO level at negative polarity (V = −1.2 V) situated at 0.73 eV below the Fermi level (ε_{0-} = −0.73 eV, *cf.* eqn (2)). This makes the current at positive polarity larger, $I_+ > |I_-|$, and yields an RR larger than unity (RR (1.5 V) $\approx$ 3, *cf.* Fig. 2C). To be sure, the above analysis makes it clear that the asymmetric values of the HOMO coupling strengths to substrate and tip ($\Gamma_{\text{s}} \neq \Gamma_{\text{t}}$) plays absolutely no role for the rectification properties of our CnT and OPTn junctions. See ref. 35 for a thorough discussion of this point.

Impact of mechanical stretching on the current rectification in CnT and OPTn junctions

As noted in the Results section, the dependence of rectification on stretching for CnT and OPTn junctions is very different. The CnT junctions show essentially no dependence of RR or γ on stretching, whereas for OPTn RR $\to$ 1 and $\gamma \to 0$ on stretching. The explanation for these two very different behaviors must lie with the different rectification mechanisms at play.

As just discussed, rectification in CnT junctions is due to the junction electric field causing Stark shifts in the energy of the highly localized HOMO orbital near the substrate. This Stark shift is insensitive to stretching of CnT because the HOMO spatial distribution is so highly localized to the C–S bond and the majority of the molecular elongation occurs in the extended C–C backbone. We have reported previously that mechanical stretching affects charge transport in CnT junctions as if the carbon backbone is a structureless medium merely described by its length;[57] the length dependence of the low bias conductance G of mechanically stretched CnT junctions cannot be distinguished from the length dependence obtained by adding –CH$_2$– repeat units in the CnT homologous series (Fig. 3a of ref. 57). This prior result means that the localized HOMO is not significantly perturbed by stretching. The independence of RR and γ on stretching is just another manifestation of the same concept.

For OPTn, on the other hand, the HOMO is delocalized over the whole molecule and low bias conductance G is very sensitive to stretching.[57] Therefore, it seems intuitively reasonable that the strong impact of stretching on G should also manifest in stretching dependence of RR and γ for OPTn. Experimental data confirm this expectation.

The mechanism discussed above for rectification in OPTn junctions is the potentiometer mechanism, *i.e.*, the convolution of the potential profile (field) and the spatial distribution of the orbital. Specifically, according to eqn (8), rectification can be affected by stretching *via* its impact on the HOMO distribution $\rho(x,y,z)$ and (or) on the potential profile $v(x,y,z)$.

We first examined whether the shape of the potential profile changes upon molecule stretching. The results of quantum chemical calculations for the microscopic potential $v(z)$ as a function of z normalized to molecule's length d (which varies upon stretching) presented in Fig. S7 and S8† reveal that this is not the case. The linear trend in the coarse

grain average $\bar{v}(z)$ of compressed and stretched OPT3 (Fig. S7A and S7B,† respectively) is similar to that in the absence of mechanical deformation, Fig. 7B and C. The changes caused by stretching manifest themselves in a weak dependence of κ on stretching. At the limits of compressive and tensile forces sampled in experiment, we estimate $\kappa \approx 3.41$ and $\kappa \approx 3.58$, respectively (*cf.* Fig. S7†).

Having determined that the impact on the potential profile shape is negligible, what remains is that the spatial distribution of the delocalized HOMO in OPTn should be significantly affected by stretching. If the distribution were to become more symmetric with respect to the center of the junction, then this would cause γ and RR to decrease. Our quantum chemical calculations demonstrate that this is indeed the case. They show that a compressive force displaces the HOMO distribution towards the thiol end. In contrast, the HOMO distribution of an elongated OPTn molecule subject to a tensile force is displaced in opposite direction and eventually reaches the center, a situation wherein current rectification disappears. Qualitatively, this is depicted in Fig. 6B and C, respectively. Quantitatively, this can be seen in Fig. 8. The black and red lines in Fig. 8A reveal, by elongating the OPT3 molecule, the fractional HOMO charge position relative to the thiol end $(z_{HOMO} - z_S)/(z_C - z_S)$ increases with the concomitant decrease of its position relative to the opposite end $(z_C - z_{HOMO})/(z_C - z_S)$.

The impact of the OPT3 molecule elongation on γ is shown in Fig. 8B (see also Fig. S9†), where curves for γ computed using the conventional and corrected potentiometer rule (eqn (5) and (11), respectively) are depicted along with the "exact" curve *via* eqn (8). As the case for nonstretched junctions, when corrected to properly account for intramolecular screening (*via* κ), γ-values based on the corrected potentiometer rule (γ_{corrPR}) agree very well with the exact ones. More to the point, the trend exhibited by the theoretical curve for γ of Fig. 8B
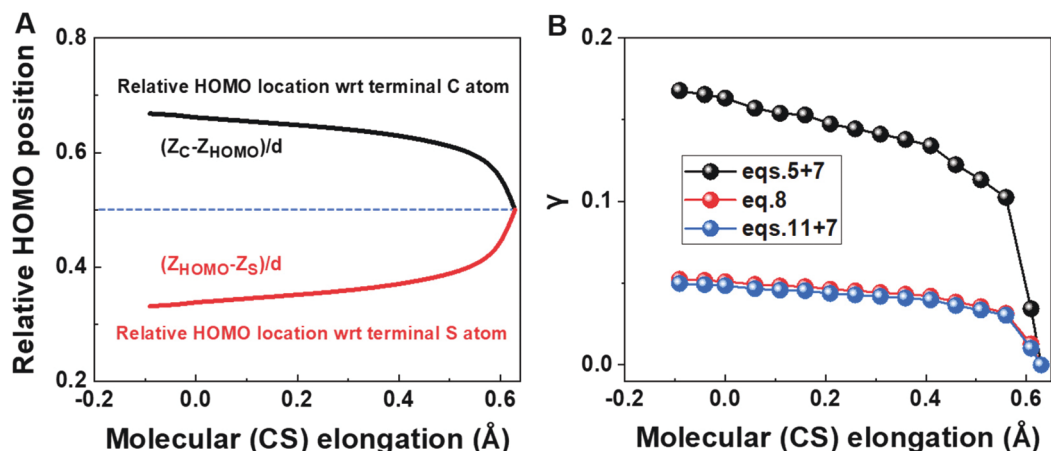

Fig. 8 Impact of stretching on the HOMO of OPT3 and the corresponding potentiometer rule prediction of γ. (A) A tensile mechanical force F causing elongation of OPT3 shifts the HOMO location, which is closer to the thiol end at $F = 0$, towards the molecular center (0.5 on the y-axis is the middle of the molecule). (B) Corresponding potentiometer rule prediction of γ vs. elongation for OPT3 obtained by means of quantum chemical calculations using equations indicated in the inset.
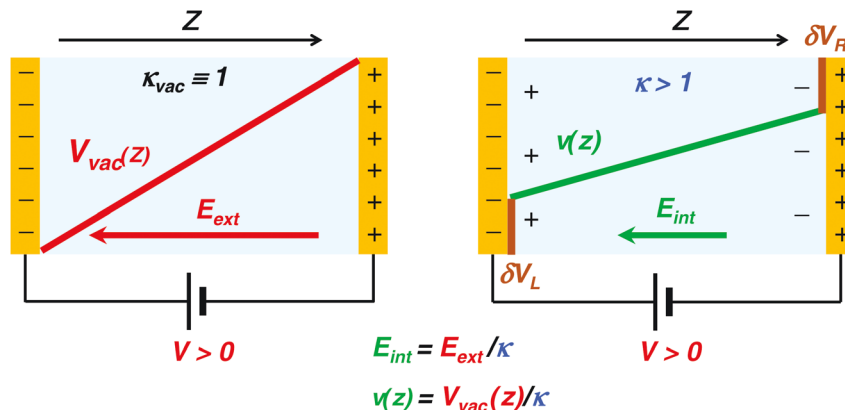
Fig. 9 Cartoon illustrating that the potential drop at interfaces arises due to screening effects regardless the fact that electrodes are ideal conductors or not and regardless whether the potential drops $\delta V_{L,R}$ at the interfaces are equal or not. The potential drops are depicted here equal ($\delta V_L = \delta V_R$) as appropriate for a plane condenser with infinite parallel plates, but they are in general not equal for molecular junctions usually having electrodes with asymmetric shapes.

deduced from quantum chemical calculations reproduces the experimental behavior of γ of Fig. 3F. Noteworthy is the slow decrease in γ in the beginning of the stretching process followed by a considerably more rapid drop as the (rupture) point is approached where rectification eventually disappears.

Dielectric screening and potential drop at the contacts

The computed potential profiles shown in Fig. 7 provide important insight into the relationship between intramolecular screening and the potential drop at the contacts. Due to intramolecular screening ($\kappa > 1$), the molecules feel merely a fraction of the applied bias $V = V_{\text{junction}}$ ($V_{\text{molecule}} = V_{\text{junction}}/\kappa$, $cf.$ eqn (9)), and this necessarily implies a potential drop of $\delta V_s + \delta V_t = V_{\text{junction}} - V_{\text{molecule}} = V(1 - 1/\kappa)$ at the contacts, Fig. 7B and C. It is important to note that this intramolecular screening effect by no means implies "bad" contacts. This can be understood if one considers a classical analogue depicted in Fig. 9. Potential drop at electrode-dielectric interfaces arises not because metal electrodes are good or bad conductors; rather, it is due to electron redistribution within the (dielectric) medium which screens the external field. To be sure, the analogy of the junction with the case in Fig. 9 should be taken with a grain of salt: because the HOMO distribution has a small tail penetrating into electrodes (which is neglected here, as noted above), a certain dependence of κ on the nature of metals used as electrodes may exist. Still, based on the analysis of the preceding subsection, we do not expect this dependence to be strong, unlike other transport properties ($e.g.$, G_s) which do exhibit a strong dependence on metal.[4,41–43,62,67,68] (RR can depend on metal because it also depends on ε_h.).

Notice that the present value $\kappa \approx 3.4$ is comparable to dielectric constants of common organic substances, and in line with previous reported value for organothiolate SAMs.[69–72] The fact that it is somewhat larger than, $e.g.$, $\kappa \approx 2.27$ (benzene) or $\kappa \approx 2.53$ (biphenyl) may be understood: $\kappa \approx 3.4$ quantifies screening effects within a single OPT3 molecule (more precisely, exactly as these effects are felt by the HOMO,

see above) and not a spatial average over the entire OPT3 SAM, which includes molecules and intermolecular "vacuum", as in the case of bulk fluid benzene or solid biphenyl.

Conclusions

In summary, experimental transport measurements on CnT and OPTn molecular junctions show that both types of junctions are weakly rectifying but that the rectification directions are opposite to each other. Furthermore, the changes in rectification ratio RR upon mechanical stretching of the junctions are very different: rectification for OPTn molecules collapses on stretching, whereas rectification in CnT is essentially independent of elongation. The rectification behavior for both types of junctions in the stretched and unstretched states can be quantitatively described by the single level model. The energy level shift coefficient γ extracted from the single level analysis is the key parameter for describing the rectification behavior in simple junctions with single step tunneling. We find that for CnT junctions $\gamma < 0$ while for OPTn junctions $\gamma > 0$, which reflects the different rectification mechanisms operating in these two junctions. Using OVGF calculations we show that the energy of the localized HOMO in isolated CnT molecules exhibits a strong Stark effect that can account for $\gamma < 0$ in this system and thus the observed rectification. However, similar OVGF calculations on isolated OPTn molecules show no strong Stark effect and we conclude that in this system rectification is due to spatial coupling of the HOMO center of charge with the potential profile in the junction, $i.e.$, the potentiometer formalism is the correct picture for rectification in OPTn. Indeed, quantum chemical calculations of the convolution of the HOMO charge with the screened potential profile in the junctions yield a theoretical value of γ that agrees extremely well with the measured value. Such calculations also can account for the observed collapse in γ upon stretching OPTn molecules. Finally, the quantum-chemically computed poten-

tial profiles provide insight into dielectric screening effects in OPT*n* junctions, and demonstrate that the fields felt by the molecules are approximately one third of nominal value based on the applied potential.

Overall, our combined experimental and theoretical analysis of rectification in C*n*T and OPT*n* molecular junctions provides new insight into the transport mechanisms operative in these systems. Our analysis also demonstrates clearly that quantitative description of the *I–V* behavior is achievable with a compact analytical model supported by quantum chemical calculations. We anticipate that these findings will aid ongoing efforts in the community to design molecular systems with functional *I–V* behavior.

Conflicts of interest

The authors declare no competing financial interests.

Acknowledgements

References

1 A. Aviram and M. A. Ratner, *Chem. Phys. Lett.*, 1974, **29**, 277–283.

2 M. L. Chabinyc, X. Chen, R. E. Holmlin, H. Jacobs, H. Skulason, C. D. Frisbie, V. Mujica, M. A. Ratner, M. A. Rampi and G. M. Whitesides, *J. Am. Chem. Soc.*, 2002, **124**, 11730–11736.

3 G. M. Morales, P. Jiang, S. Yuan, Y. Lee, A. Sanchez, W. You and L. Yu, *J. Am. Chem. Soc.*, 2005, **127**, 10456–10457.

4 Z. Xie, I. Bâldea and C. D. Frisbie, *Chem. Sci.*, 2018, **9**, 4456–4467.

5 L. Yuan, R. Breuer, L. Jiang, M. Schmittel and C. A. Nijhuis, *Nano Lett.*, 2015, **15**, 5506–5512.

6 R. M. Metzger, *Chem. Rev.*, 2015, **115**, 5056–5115.

7 D. Xiang, X. Wang, C. Jia, T. Lee and X. Guo, *Chem. Rev.*, 2016, **116**, 4318–4440.

8 W. Lo, N. Zhang, Z. Cai, L. Li and L. Yu, *Acc. Chem. Res.*, 2016, **49**, 1852–1863.

9 Y. Ai, A. Kovalchuk, X. Qiu, Y. Zhang, S. Kumar, X. Wang, M. Kühnel, K. Nørgaard and R. C. Chiechi, *Nano Lett.*, 2018, **18**, 7552–7559.

10 Y. Cai, A. Zhang, Y. Feng and C. Zhang, *J. Chem. Phys.*, 2011, **135**, 184703.

11 J. Shin, S. Yang, Y. Jang, J. S. Eo, T. W. Kim, T. Lee, C. H. Lee and G. Wang, *Nat. Commun.*, 2020, **11**, 1412.

12 L. Yuan, N. Nerngchamnong, L. Cao, H. Hamoudi, E. Del Barco, M. Roemer, R. K. Sriramula, D. Thompson and C. A. Nijhuis, *Nat. Commun.*, 2015, **6**, 6324.

13 I. Díez-Pérez, J. Hihath, Y. Lee, L. Yu, L. Adamska, M. A. Kozhushner, I. I. Oleynik and N. Tao, *Nat. Chem.*, 2009, **1**, 635–641.

14 C. A. Nijhuis, W. F. Reus and G. M. Whitesides, *J. Am. Chem. Soc.*, 2009, **131**, 17814–17827.

15 J. Hihath, C. Bruot, H. Nakamura, Y. Asai, I. Díez-Pérez, Y. Lee, L. Yu and N. Tao, *ACS Nano*, 2011, **5**, 8331–8339.

16 E. Lortscher, B. Gotsmann, Y. Lee, L. Yu, C. Rettner and H. Riel, *ACS Nano*, 2012, **6**, 4931–4939.

17 A. Batra, P. Darancet, Q. Chen, J. S. Meisner, J. R. Widawsky, J. B. Neaton, C. Nuckolls and L. Venkataraman, *Nano Lett.*, 2013, **13**, 6233–6237.

18 N. Zhang, W. Y. Lo, Z. Cai, L. Li and L. Yu, *Nano Lett.*, 2017, **17**, 308–312.

19 C. Van Dyck and M. A. Ratner, *Nano Lett.*, 2015, **15**, 1577–1584.

20 M. Souto, L. Yuan, D. C. Morales, L. Jiang, I. Ratera, C. A. Nijhuis and J. Veciana, *J. Am. Chem. Soc.*, 2017, **139**, 4262–4265.

21 B. Capozzi, J. Xia, O. Adak, E. J. Dell, Z. F. Liu, J. C. Taylor, J. B. Neaton, L. M. Campos and L. Venkataraman, *Nat. Nanotechnol.*, 2015, **10**, 522–527.

22 Q. Van Nguyen, P. Martin, D. Frath, M. L. Della Rocca, F. Lafolet, C. Barraud, P. Lafarge, V. Mukundan, D. James, R. L. McCreery and J. C. Lacroix, *J. Am. Chem. Soc.*, 2017, **139**, 11913–11922.

23 A. Bayat, J.-C. Lacroix and R. L. McCreery, *J. Am. Chem. Soc.*, 2016, **138**, 12287–12296.

24 J. Taylor, M. Brandbyge and K. Stokbro, *Phys. Rev. Lett.*, 2002, **89**, 138301.

25 Y. Han, M. S. Maglione, V. Diez-Cabanes, J. Casado-Montenegro, X. Yu, S. K. Karuppannan, Z. Zhang, N. Crivillers, M. Mas-Torrent, C. Rovira, J. Cornil, J. Veciana and C. A. Nijhuis, *ACS Appl. Mater. Interfaces*, 2020, **12**, 55044–55055.

26 X. Chen, M. Roemer, L. Yuan, W. Du, D. Thompson, E. Del Barco and C. A. Nijhuis, *Nat. Nanotechnol.*, 2017, **12**, 797–803.

27 J. Park, L. Belding, L. Yuan, M. P. S. Mousavi, S. E. Root, H. J. Yoon and G. M. Whitesides, *J. Am. Chem. Soc.*, 2021, **143**, 2156–2163.

28 C. Van Dyck and A. J. Bergren, *Adv. Electron. Mater.*, 2018, **4**, 1–10.

29 F. Von Wrochem, D. Gao, F. Scholz, H. G. Nothofer, G. Nelles and J. M. Wessels, *Nat. Nanotechnol.*, 2010, **5**, 618–624.

30 H. J. Yoon, K. C. Liao, M. R. Lockett, S. W. Kwok, M. Baghbanzadeh and G. M. Whitesides, *J. Am. Chem. Soc.*, 2014, **136**, 17155–17162.

31 L. Luo, L. Balhorn, B. Vlaisavljevich, D. Ma, L. Gagliardi and C. D. Frisbie, *J. Phys. Chem. C*, 2014, **118**, 26485–26497.

32 S. K. Yee, J. Sun, P. Darancet, T. D. Tilley, A. Majumdar, J. B. Neaton and R. A. Segalman, *ACS Nano*, 2011, **5**, 9256–9263.

33 M. Souto, V. Díez-Cabanes, L. Yuan, A. R. Kyvik, I. Ratera, C. A. Nijhuis, J. Cornil and J. Veciana, *Phys. Chem. Chem. Phys.*, 2018, **20**, 25638–25647.

34 D. Gao, F. Scholz, H. G. Nothofer, W. E. Ford, U. Scherf, J. M. Wessels, A. Yasuda and F. Von Wrochem, *J. Am. Chem. Soc.*, 2011, **133**, 5921–5930.

35 I. Bâldea, *Phys. Rev. B*, 2021, **103**, 195408.

36 G. Zhang, M. A. Ratner and M. G. Reuter, *J. Phys. Chem. C*, 2015, **119**, 6254–6260.

37 S. Datta, *Electronic Transport in Mesoscopic Systems*, Cambridge University Press, Cambridge, UK, 1999.

38 S. M. Sze, *Physics of Semiconductor Devices*, John Wiley & Sons, New York, USA, 1981.

39 I. Bâldea, *Chem. Phys.*, 2010, **377**, 15–20.

40 I. Bâldea, *Phys. Rev. B: Condens. Matter Mater. Phys.*, 2012, **85**, 035442.

41 C. E. Smith, Z. Xie, I. Bâldea and C. D. Frisbie, *Nanoscale*, 2018, **10**, 964–975.

42 Z. Xie, I. Bâldea and C. D. Frisbie, *J. Am. Chem. Soc.*, 2019, **141**, 3670–3681.

43 Z. Xie, I. Baldea and C. D. Frisbie, *J. Am. Chem. Soc.*, 2019, **141**, 18182–18192.

44 Q. Van Nguyen, Z. Xie and C. D. Frisbie, *J. Phys. Chem. C*, 2021, **125**, 4292–4298.

45 H. Kang, G. D. Kong, S. E. Byeon, S. Yang, J. W. Kim and H. J. Yoon, *J. Phys. Chem. Lett.*, 2020, **11**, 8597–8603.

46 W. Wang, T. Lee and A. Reed, *Phys. Rev. B: Condens. Matter Mater. Phys.*, 2003, **68**, 035416.

47 T. W. Kim, G. Wang, H. Lee and T. Lee, *Nanotechnology*, 2007, **18**, 315204.

48 A. J. Kronemeijer, E. H. Huisman, H. B. Akkerman, A. M. Goossens, I. Katsouras, P. A. Van Hal, T. C. T. Geuns, S. J. Van Der Molen, P. W. M. Blom and D. M. De Leeuw, *Appl. Phys. Lett.*, 2010, **97**, 173302.

49 S. J. Cho, G. D. Kong, S. Park, J. Park, S. E. Byeon, T. Kim and H. J. Yoon, *Nano Lett.*, 2019, **19**, 545–553.

50 F. Zahid, M. Paulsson and S. Datta, Electrical conduction through molecules, in *Advanced semiconductors and organic nano-techniques*, Academic Press, New York, 2003, vol. 3.

51 I. Bâldea, *Phys. Chem. Chem. Phys.*, 2015, **17**, 31260–31269.

52 A. M. Kuznetsov and J. Ulstrup, *J. Phys. Chem. A*, 2000, **104**, 11531–11540.

53 I. R. Peterson, D. Vuillaume and R. M. Metzger, *J. Phys. Chem. A*, 2001, **105**, 4702–4707.

54 J. Zhang, Q. Chi, A. M. Kuznetsov, A. G. Hansen, H. Wackerbarth, H. E. M. Christensen, J. E. T. Andersen and J. Ulstrup, *J. Phys. Chem. B*, 2002, **106**, 1131–1152.

55 J. Zhang, A. M. Kuznetsov and J. Ulstrup, *J. Electroanal. Chem.*, 2003, **541**, 133–146.

56 Z. Xie, I. Bâldea, A. T. Demissie, C. E. Smith, Y. Wu, G. Haugstad and C. D. Frisbie, *J. Am. Chem. Soc.*, 2017, **139**, 5696–5699.

57 Z. Xie, I. Bâldea, G. Haugstad and C. D. Frisbie, *J. Am. Chem. Soc.*, 2019, **141**, 497–504.

58 L. S. Cederbaum and W. Domcke, in *Advances in Chemical Physics*, ed. I. Prigogine and S. A. Rice, John Wiley & Sons Inc, New York, London, Sydney, Toronto, 1977, vol. 36, pp. 205–344.

59 W. von Niessen, J. Schirmer and L. S. Cederbaum, *Comput. Phys. Rep.*, 1984, **1**, 57–125.

60 M. J. Frisch, G. W. Trucks, H. B. Schlegel, G. E. Scuseria, M. A. Robb, J. R. Cheeseman, G. Scalmani, V. Barone, G. A. Petersson, H. Nakatsuji, X. Li, M. Caricato, A. V. Marenich, J. Bloino, B. G. Janesko, R. Gomperts, B. Mennucci, H. P. Hratchian, J. V. Ortiz, A. F. Izmaylov, J. L. Sonnenberg, D. Williams-Young, F. Ding, F. Lipparini, F. Egidi, J. Goings, B. Peng, A. Petrone, T. Henderson, D. Ranasinghe, V. G. Zakrzewski, J. Gao, N. Rega, G. Zheng, W. Liang, M. Hada, M. Ehara, K. Toyota, R. Fukuda, J. Hasegawa, M. Ishida, T. Nakajima, Y. Honda, O. Kitao, H. Nakai, T. Vreven, K. Throssell, J. A. Montgomery, J. E. P. Jr., F. Ogliaro, M. J. Bearpark, J. J. Heyd, E. N. Brothers, K. N. Kudin, V. N. Staroverov, T. A. Keith, R. Kobayashi, J. Normand, K. Raghavachari, A. P. Rendell, J. C. Burant, S. S. Iyengar, J. Tomasi, M. Cossi, J. M. Millam, M. Klene, C. Adamo, R. Cammi, J. W. Ochterski, R. L. Martin, K. Morokuma, O. Farkas, J. B. Foresman and D. J. Fox, *Gaussian 16, Revision B.01*, Gaussian, Inc., Wallingford CT, 2016.

61 bwHPC and bwHPC-C5 (http://www.bwhpc-c5.de) funded by the Ministry of Science, Research and the Arts Baden-Württemberg, the Universities of the State Baden-Württemberg, and the German Research Foundation (DFG).

62 Z. Xie, I. Bâldea, C. E. Smith, Y. Wu and C. D. Frisbie, *ACS Nano*, 2015, **9**, 8022–8036.

63 L. S. Cederbaum, *J. Phys. B: At. Mol. Phys.*, 1975, **8**, 290–303.

64 J. A. Malen, P. Doak, K. Baheti, T. Don Tilley, R. A. Segalman and A. Majumdar, *Nano Lett.*, 2009, **9**, 1164–1169.

65 C. Li, I. Pobelov, T. Wandlowski, A. Bagrets, A. Arnold and F. Evers, *J. Am. Chem. Soc.*, 2008, **130**, 318–326.

66 H. Song, Y. Kim, Y. H. Jang, H. Jeong, M. A. Reed and T. Lee, *Nature*, 2009, **462**, 1039–1043.

67 G. Wang, T. Kim, Y. H. Jang and T. Lee, *J. Phys. Chem. C*, 2008, **112**, 13010–13016.

68 T. Kim, H. Vázquez, M. S. Hybertsen and L. Venkataraman, *Nano Lett.*, 2013, **13**, 3358–3364.

69 C. S. S. Sangeeth, A. Wan and C. A. Nijhuis, *J. Am. Chem. Soc.*, 2014, **136**, 11134–11144.

70 L. Jiang, C. S. S. Sangeeth and C. A. Nijhuis, *J. Am. Chem. Soc.*, 2015, **137**, 10659–10667.

71 P. Song, D. Thompson, H. V. Annadata, S. Guerin, K. P. Loh and C. A. Nijhuis, *J. Phys. Chem. C*, 2017, **121**, 4172–4180.

72 C. S. S. Sangeeth, A. T. Demissie, L. Yuan, T. Wang, C. D. Frisbie and C. A. Nijhuis, *J. Am. Chem. Soc.*, 2016, **138**, 7305–7314.